Article

Lensed Fiber-Optic Two-Photon Endomicroscopy for Field-of-View Enhancement

Conghao Wang [1], Huilan Liu [1,2], Jianrui Ma [1], Qiang Fu [3], Yijun Li [3], Yanchuan Chen [3], Yuqian Gao [3], Jingquan Tian [3], Xinlei Luo [3], Fei Yu [4,5], Chunzhu Zhao [6], Runlong Wu [6], Aimin Wang [7] and Lishuang Feng [1,2,8,*]

1   School of Instrumentation and Optoelectronic Engineering, Beihang University, Beijing 100191, China; conghaowang@buaa.edu.cn (C.W.)
2   Key Laboratory of Precision Opto-Mechatronics Technology (Ministry of Education), Beijing 100191, China
3   Beijing Transcend Vivoscope Biotech Co., Ltd., Beijing 100049, China
4   Hangzhou Institute for Advanced Study, University of Chinese Academy of Sciences, Hangzhou 310024, China
5   Key Laboratory of Materials for High Power Laser, Shanghai Institute of Optics and Fine Mechanics, Chinese Academy of Sciences, Shanghai 201800, China
6   National Biomedical Imaging Center, State Key Laboratory of Membrane Biology, Institute of Molecular Medicine, Peking-Tsinghua Center for Life Sciences, College of Future Technology, Peking University, Beijing 100871, China
7   State Key Laboratory of Advanced Optical Communication System and Networks, School of Electronics, Peking University, Beijing 100871, China
8   Laboratory of Intelligent Sensing Materials and Chip Integration Technology of Zhejiang Province, Hangzhou Innovation Institute of Beihang University, Hangzhou 310063, China
*   Correspondence: fenglishuang@buaa.edu.cn

Abstract: Two-photon endomicroscopy is a promising technique with the ability to achieve in situ imaging and diagnosis at subcellular resolution. The large field-of-view capability is essential and useful to locate and image suspicious areas of biological tissue. In this work, we report objective-lens-free, lensed fiber-optic two-photon endomicroscopy for field-of-view enhancement. The field of view of this two-photon endomicroscopic probe is 750 μm with a resolution of 3.03 μm. This 1.6 g miniature probe has an integrated outer diameter of 5.8 mm and a rigid length of 33.5 mm. The imaging performance of the lensed-fiber-optic two-photon endomicroscopy was validated by examining an ex vivo mouse heart, kidney, brain, stomach wall tissues, and in vivo brain tissue.

Keywords: two-photon endomicroscopy; lensed fiber; field-of-view enhancement

1. Introduction

Two-photon microscopy (TPM) has been widely used in life sciences since its invention in the 1990s [1,2]. Its advantages include optical sectioning capacity, deep penetration depth, and label-free structural/metabolic imaging. Recent developments in miniature TPM have enabled researchers to take this highly integrated and lightweight platform to explore more application paradigms, especially the brain imaging in freely behaving animals [3–6]. Fiber-optic two-photon endomicroscopy (TPEM) is one of the crucial branches of miniature TPM, and typical distal-scanning endomicroscopic probe configurations, such as MEMS (micro-electromechanical) scanning scheme [7–9] and the piezoelectric tube (PZT) fiber-scanning scheme [10–20], have been developed. The PZT fiber-scanning distal scanning scheme could share a single double-cladding fiber (DCF) for common-path femtosecond pulse excitation and fluorescence transmission, which is potentially more advantageous for probe integration. The fiber-optic TPEM is a promising endomicroscopic technique that performs the in vivo optical biopsy of biological tissues with histological resolution, which offers the diagnostic and translational potential in gastrointestinal [21] and brain [22] diseases.

Most of the reported TPEMs use stationary micro-objectives with magnification (M) >1 to focus. Limited by the fixed spatial bandwidth of the objective, the field-of-view (FOV)

is 1/M of the PZT fiber scanner scanning range (D_{scan}), resulting in a FOV of less than 500 μm [10–20]. However, in actual clinical applications, a larger FOV is essential and helpful to locate and image suspicious areas of biological tissue. The lensed fiber technique has been applied by several groups in fiber-optic endomicroscopy due to its objective-lens-free direct imaging capability, flexible parameter optimization, and compatibility for miniature probe integration [23–25]. The superior advantage of lensed fiber-optic imaging without the stationary objective lens solution is that the actual FOV is D_{scan}, thus realizing an M-fold enhancement in FOV.

Several research groups have explored the direct imaging capability with a lensed fiber in the confocal and multi-photon endomicroscopic imaging field. In 2009, Bao et al. [26] realized the imaging validation of the hemisphere-lensed fiber for two-photon imaging with no objective lens for the first time. The numerical aperture (NA) of this lensed fiber is 0.12 and its corresponding focal spot is 6 μm. Two-photon fluorescent images of 10 μm microspheres can be obtained. In 2018, Akhoundi et al. [27] demonstrated a large FOV (>600 μm) 1700 nm excited multiphoton endoscopy prototype with 2.2 μm lateral resolution by gluing the stationary objective lens in front of DCF. The PZT drives the overall structure to achieve spiral scanning, thus resulting in a lower frame rate (15 s/frame). The integrated endoscopy probe has an 5 mm outer diameter and 40 mm rigid length. In 2021, Kim et al. [28] reported an objective-lens-free, 2.6 mm packaged diameter, Lissajous scanning confocal endomicroscopy with a PZT-driven hemisphere-lensed fiber. The lensed fiber is composed of the single-mode fiber and coreless silica fiber segment. A hemisphere is manufactured on the tip of the fiber by the arc discharge of the fusion splicer, which acts as a focusing objective lens. This scheme has verified the feasibility of using a hemisphere-lensed fiber to achieve a large FOV (>400 μm) and 2.6 μm lateral resolution in fiber-scanning confocal endomicroscopy. Considering the more stringent conditions for femtosecond pulse delivery and fluorescence signal collection, the fabrication of lensed fiber for two-photon endomicroscopy is more challenging. Additionally, from the current state of the art, the FOV enhancement capability using lensed fiber in the PZT fiber-scanning TPEM scheme has not been verified yet.

In this work, we report an objective-lens-free, lensed fiber-optic TPEM scheme for field-of-view enhancement. The FOV of this two-photon endomicroscopic probe is 750 μm with a resolution of 3.03 μm. Firstly, in the theoretical part, the ABCD transformation matrix of the lensed fiber based on hollow-core antiresonant fiber is established. The effects of the hemisphere radius and LCF length on the focused waist radius, working distance and NA are analyzed. Secondly, in the experimental part, the engineered fabrication of the lensed fiber, based on arc discharge, is carried out. The far-field NA and near-field spot size of the lensed fiber are measured. Finally, the performance of this lensed fiber-optic TPEM probe (5.8 mm outer diameter, 33.5 mm rigid length) is validated by examining ex vivo mouse heart, kidney, brain, stomach wall and in vivo brain tissue.

2. Methods

2.1. Lensed Fiber-Optic Two-Photon Endomicroscopy Setup Overview

Figure 1a illustrates the structure of our objective-lens-free, lensed fiber-optic TPEM. More theoretical and experimental details about the fiber-scanning TPEM platform can also be found in our previous reports [20,29–32]. In brief, the 920 nm femtosecond fiber laser with an 80 MHz repetition rate is chosen as the TPEM laser source. The femtosecond pulse passes through the dichroic mirror (DM; DMLP650R, Thorlabs, Newton, NJ, USA) and is then coupled into a custom-made double-cladding antiresonant fiber (DC-ARF) through the aspheric coupling lens (CL; 354850 B, Lightpath, Orlando, FL, USA). The DC-ARF has a geometric hollow-core and cladding diameter of 24 μm and 134 μm, respectively. The NA values of the DC-ARF core and cladding are 0.034 and 0.5, respectively. The group velocity dispersion (GVD) and transmission loss measured at 920 nm is 5.5 ps/km/nm and 0.1 dB/m [29], showing more excellent dispersion and transmission characteristics than the photonic crystal bandgap fiber [30], therefore no additional dispersion compensation

devices (i.e., grating pairs and prism pairs) are used in this platform. The laser pulses are transmitted to the miniaturized TPEM via the DC-ARF core and used to excite two-photon fluorescence for biological tissue. The two-photon fluorescence is collected backwards through the DC-ARF cladding, bandpass filter (FF01-530/43-25, Semrock, West Henrietta, NY, USA), collection lens (LA1951-A, Thorlabs, Newton, NJ, USA), and converges to the photomultiplier tube (PMT; H10770PA-40-SEL, Hamamatsu, Shizuoka Prefecture, Japan) for subsequent digital signal acquisition and reconstruction.

The integrated TPEM probe has an outer diameter of 5.8 mm, a rigid length of 33.5 mm, and a weight of 1.6 g, as depicted in Figure 1b. This lightweight probe is composed of the custom-made reverse-fixed PZT (PT230.94, Physik Instruments, Karlsruhe, Germany) fiber scanner and lensed fiber. The front end of the probe is encapsulated with a 5 mm diameter, 100 μm thick glass window to protect the scanning lensed fiber and meet the actual needs for ex vivo and in vivo biological imaging. The four-quadrant PZT has a 3.2 mm outer diameter, 2.2 mm inner diameter, and 30 mm length. To reduce the rigid length of the integrated probe, the PZT and lensed fiber form a reverse-fixed structure [32,33]. By applying and sweeping sine and cosine voltage signals amplified by voltage amplifier (TD250, Piezodrive, Shortland, Australia) to the PZT fiber scanner and monitoring the scanning track by CMOS camera (Panda, 4.2 M PCO, Kelheim, Germany), the second-order resonant point of this 30.5 mm cantilever PZT scanner is obtained to be approximately 660 Hz. In our TPEM platform, 512-ring two-dimensional spiral scanning trajectories are achieved by the synchronous amplitude-modulated sine and cosine voltage signals acting on the scanner, which are generated by the field programmable gate array control circuit. The scanning period of a PZT scanner mainly consists of an increased amplitude period (512 rings) and a decreased amplitude period (512 rings). The increased amplitude period is used for two-photon endoscopic imaging, corresponding to an imaging frame rate of approximately 0.65 fps. To achieve the correction of the elliptical trajectory to the circular trajectory, we adjust the drive voltages of the X and Y axes, and finely tune the drive phase x. More detailed content of the trajectory correction method can also be found in our previous work [29].

As the most critical optical device within this TPEM platform, the lensed fiber (depicted in Figure 1c) is obtained through DC-ARF and a large-core multimode fiber (LCF) fusion, fixed-length cutting, and the discharge generation of hemisphere surfaces. The geometric length of LCF, and the radius of the hemisphere surface in this lensed fiber is approximately 0.906 mm and 82 μm, respectively. The gradient step refractive index distribution LCF (SI 105/125-22/250, Yangtze Optical Fibre and Cable, Wuhan, China) has a geometric core and cladding diameters of 105 μm and 125 μm, respectively, with 0.22 core NA and 8 dB/km transmission loss of at 850 nm. The LCF acts as the spacer to expand the beam size in this lensed fiber model. The scanning electron microscopy (SEM) image of DC-ARF and fiber endface microscopy image of LCF are depicted in Figure 1d,e, respectively.

2.2. ABCD Transformation Matrix Analysis of Lensed Fiber

Figure 2 depicts the geometric schematic of the lensed fiber composed of an ARF and LCF. As a typical photonic crystal fiber, ARF confines the light in the core of the fiber based on antiresonant principle [34], and has endlessly single-mode transmission characteristics [35]. The LCF acts as the spacer to expand the Gaussian beam size. The propagation of the Gaussian beam in lensed fiber is modeled using the ABCD transformation matrix [36,37]. The influence of the key parameters of the lensed fiber, such as the LCF length and hemisphere radius, are theoretically analyzed for their effects on the spot output characteristics. In the geometric model, the abbreviated symbols are as follows: R, L, n_1, n_2 is the hemisphere radius, LCF length, air refractive index, and LCF refractive index, respectively. ω_0 is the antiresonant fiber mode field radius, λ is the working wavelength.
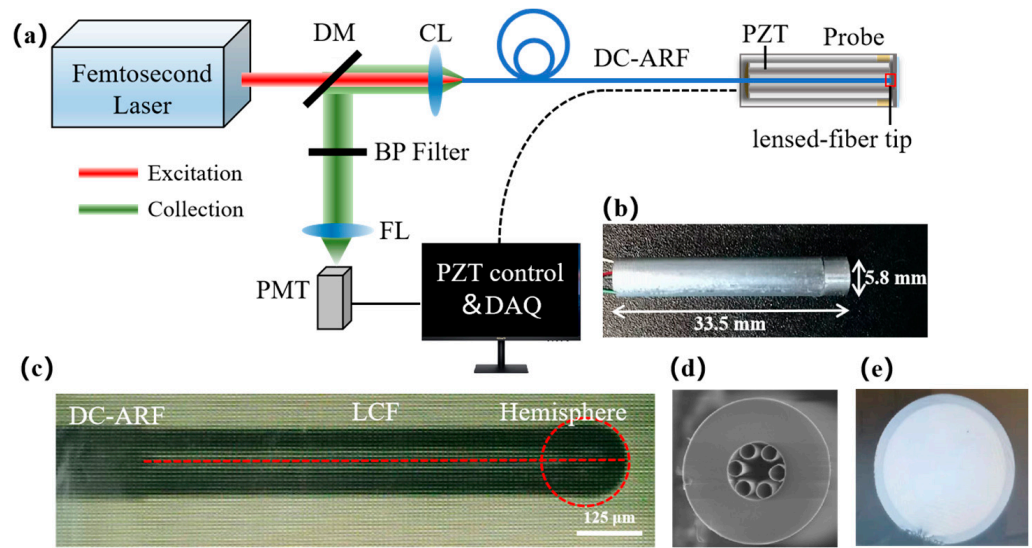
Figure 1. (**a**) Schematic of objective-lens-free fiber-optic TPEM. DM: dichroic mirror. CL: coupling lens. DC-ARF: double-cladding antiresonant fiber. PZT: piezoelectric ceramic tube. BP filter: bandpass filter. FL: focusing lens. PMT: photomultiplier tube. (**b**) Photograph of the 1.6 g integrated probe. (**c**) Photograph of the lensed fiber. (**d**) SEM image of DC-ARF. (**e**) Fiber endface microscopy image of LCF.
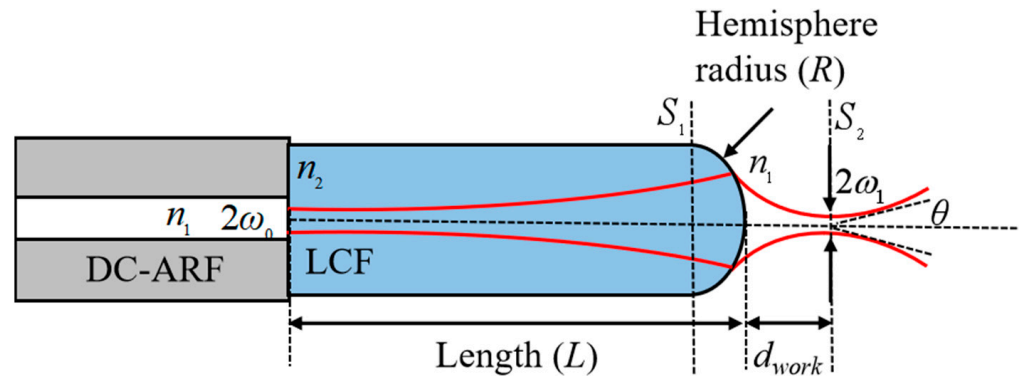

Figure 2. Geometric schematic of the lensed fiber.

The total transformation matrix T of the lensed fiber can be obtained:

$$T = T_4 T_3 T_2 T_1 = \begin{bmatrix} A & B \\ C & D \end{bmatrix} = \begin{bmatrix} 1 + (\frac{1-n}{R})d & \frac{L}{n} + d[(\frac{1-n}{R})\frac{L}{n} + 1] \\ \frac{1-n}{R} & (\frac{1-n}{R})\frac{L}{n} + 1 \end{bmatrix} \tag{1}$$

with

$$T_1 = \begin{bmatrix} 1 & 0 \\ 0 & \frac{n_1}{n_2} \end{bmatrix}, \ T_2 = \begin{bmatrix} 1 & L \\ 0 & 1 \end{bmatrix}, \ T_3 = \begin{bmatrix} 1 & 0 \\ \frac{n_1-n_2}{n_1 R} & \frac{n_2}{n_1} \end{bmatrix}, \ T_4 = \begin{bmatrix} 1 & d \\ 0 & 1 \end{bmatrix} \tag{2}$$

We point out that compared to the lensed fiber model consisting of a solid single-mode fiber with LCF [23,24,28], the T_1 transformation matrix is added to Equation (1) because the DC-ARF has a hollow core.

The input parameter q_0 of the Gaussian beam and output parameter q_1 at the waist of the lensed fiber can be expressed in Equations (3) and (4):

$$q_0 = i \frac{\pi \omega_0^2}{\lambda} \tag{3}$$

$$\frac{1}{q_1} = \frac{1}{R_1} - i \frac{\lambda}{\pi \omega_1^2} \tag{4}$$

By considering the ABCD transformation matrix of the Gaussian-beam parameter, as depicted in Equation (5):

$$q_1 = \frac{Aq_0 + B}{Cq_0 + D} \tag{5}$$

Then, Equations (3) and (4) can be combined and solved. The output waist radius (ω_1), the working distance (d) and the output NA after the lensed fiber transformation can be obtained by Equations (6)–(8):

$$\omega_1 = \frac{1}{\pi} \frac{\lambda \omega_0}{\sqrt{AD - BC}} \tag{6}$$

$$d = \frac{(\frac{n-1}{R})x^2 - \frac{L}{n}(\frac{1-n}{R}\frac{L}{n} + 1)}{(\frac{1-n}{R})^2 x^2 + (\frac{1-n}{R}\frac{L}{n} + 1)^2} \tag{7}$$

$$NA_{fiber} = \sin(\arctan(\frac{\lambda}{\pi \omega_1})) \tag{8}$$

where $x = \frac{\pi \omega_0^2}{\lambda}$.

In our two-photon endomicroscopy platform, the geometric parameters of the lensed fiber hemisphere radius R is 82 μm, LCF length L is 0.906 mm, the DC-ARF mode field radius ω_0 is 8.6 μm, and the working wavelength λ is 920 nm. By bringing the above parameters into Equations (3)–(5), we can obtain the theoretical simulation results of the output parameters of this lensed fiber, where the output waist radius ω_1 is 3.02 μm, the working distance d is 233 μm, and the output NA is 0.096. The two-dimensional simulation curves of the waist radius, working distance, and output numerical aperture are depicted in Figure 3, where the hemisphere radius of the curvature varies from 50 to 100 μm and the LCF length varies from 0.3 mm to 1.2 mm.
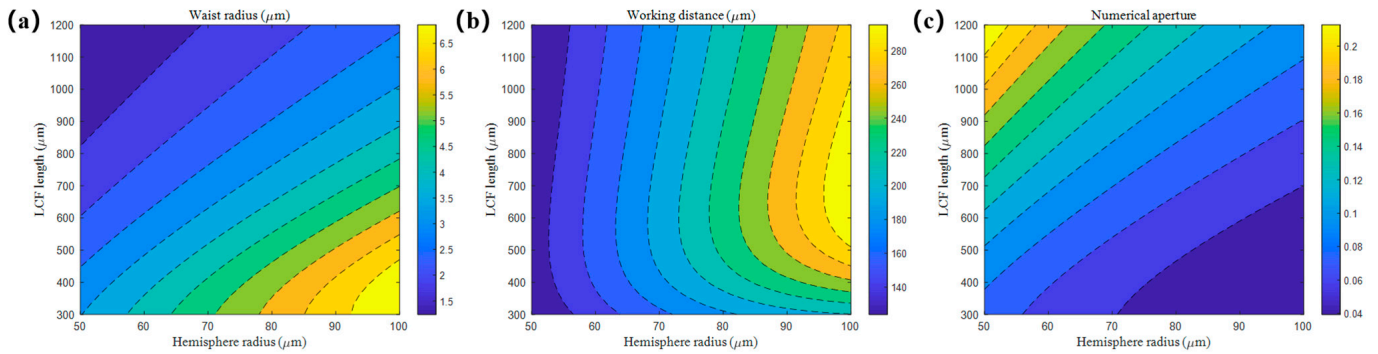

Figure 3. Simulation of the hemisphere radius and LCF length for the lensed fiber output: (**a**) waist radius; (**b**) working distance; and (**c**) numerical aperture. The dashed line in the figure is the equipotential line.

2.3. Fabrication and Evaluation of Lensed Fiber

The fabrication of the lensed fiber is critical for lightweight TPEM probe integration and two-photon imaging. Two key technical challenges are involved in this process. First, the geometric structure of the lensed fiber (LCF length and hemisphere radius) determines the final two-photon endomicroscopic imaging performance. There is a tradeoff between imaging resolution and working distance. In order to achieve the probe integration and imaging of the biological tissue at certain depth, the working distance of the lensed fiber used in such fiber-scanning TPEM should be greater than 200 μm (100 μm of which is occupied by the probe protection glass window). On this basis, the structural parameters of the lensed fiber are then optimized to ensure imaging resolution. Second, considering the common-path design of this TPEM platform, the transmission performance of the lensed fiber determines the forward femtosecond pulse transmission and reverse fluorescence collection performance at the same time. As a type of air-hole photonic crystal fiber, the

fusion conditions of ARF and LCF need to be explored. Unreasonable fusion conditions can lead to the serious collapse of the crystal fiber microstructure, which, in turn, increases the fusion loss undesirably [38–40]. Thus, the low-loss fusion of the DC-ARF to the LCF becomes the second technical challenge which need to be broken through.

Figure 4 depicts the conventional fabrication process of the lensed fiber by arc discharge for fiber-optic endomicroscopy [23,28]. The primary steps are as follows: (1) The DC-ARF is spliced into the LCF by arc discharge in a fusion splicer (FSM-100P+, Fujikura, Tokyo, Japan). Because the ARF is a hollow-core fiber, excessive discharge intensity could cause the capillary structure to collapse, increasing the splice loss. Therefore, the fusion conditions need to be finely optimized to meet the needs of the lensed fiber fabrication. The optimization process of the fusion conditions will be described in detail in the next section, and only the final fusion parameters used for lensed fiber fabrication are given here. For discharge fusion, the DC-ARF and LCF are placed in the left and right fiber holders of the fusion splicer, respectively. The lateral distance between the fusion point and the discharge electrode is referred to as the fiber offset. To reduce the splice loss, the fiber offset is set to 20 µm on the left side, which means that the fusion point is 20 µm to the left away from the discharge electrode. The main discharge intensity of the fusion splicer is 200 bit and its main discharge time is 500 ms. The 200 bit main discharge intensity corresponds to 13.2 mA discharge current. In order to increase the fusion joint strength, another four re-discharges are then performed with a discharge intensity and time of 180 bit and 800 ms, respectively. In this case, the strength of the fusion point is sufficient to meet the stress needs of later cutting. (2) To obtain a specified length, the LCF is cut using a fiber cleaver under a microscope (XTL-400, Guiguang, Guilin, China). (3–4) The LCF is discharged to generate a hemispheric surface on which the output spot is focused. We use a discharge intensity of 500 bit and a discharge time of 500 ms to fabricate the hemisphere surface.
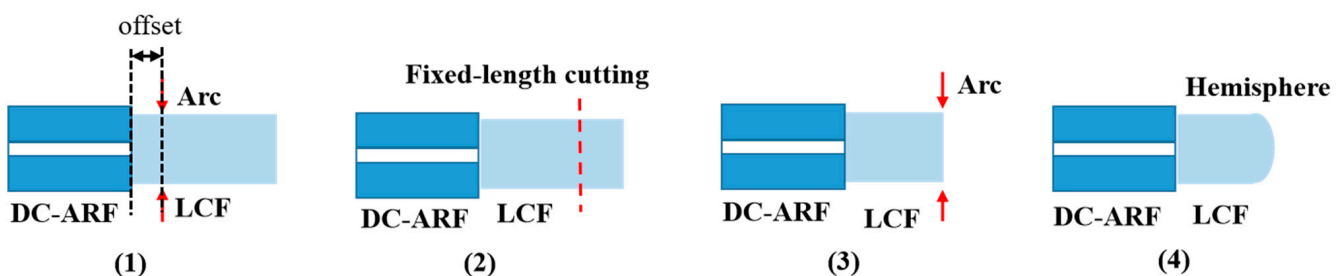

Figure 4. The fabrication process of lensed fiber.

Next, the splice loss optimization process of the DC-ARF and LCF fusion conditions is optimized precisely. The two crucial parameters, discharge intensity and fiber offset, are optimized using the DC-ARF and single-mode fiber (SMF; Hi1060, Corning, Glendale, AZ, USA). The SMF has a geometric core and cladding diameters of 5.3 µm and 125 µm, respectively, with core NA of 0.14, and transmission loss of 2.1 dB/km at 980 nm. A 915 nm continuous light source (LR-PSFJ-915/1–100 mW, Changchun Laser Technology, Changchun, China) is utilized as the laser source. The DC-ARF is first aligned with the 0.75 m SMF in the fusion splicer, and the output of the SMF is connected to a desktop power meter (HS6101A, Hongshan, Shanghai, China) for power monitoring. The output powers of the SMF before and after fusion splicing are recorded as P_1 and P_2, respectively. Consequently, the splice loss of the fusion point can be calculated using Equation (9):

$$\alpha_{loss} = -10\lg\left(\frac{P_2}{P_1}\right) \tag{9}$$

The splice loss measurements of the main discharge intensities and times between the DC-ARF and SMF are shown in Figure 5a. The main discharge, which is the first discharge, ranges in intensity from 180 to 220 bit. The main discharge time is 500 ms, which remained unchanged. The second to fifth discharges are re-discharges. Both the 180 bit re-discharge

intensity and the 800 ms discharge time remained unchanged. Throughout the discharges, the fiber offset was kept constant at 20 μm to the left. After one main discharge at 180 bit, 200 bit, 205 bit, 210 bit, 220 bit, and four re-discharges, the splice loss was 0.92 dB, 1.01 dB, 1.26 dB, 1.60 dB, and 2.23 dB, respectively. Increasing the main discharge intensity leads to a further increase in the splice loss. The splice loss measurements of the fiber offset and discharge times are shown in Figure 5b. To minimize the damage to the ARF core structure caused by excessive discharge intensity, the fusion point should be situated at a distance from the discharge electrode. For this experiment, the main discharge intensity of 200 bit and 500 ms, respectively, remained constant. From the second to fifth discharge, a re-discharge intensity and time of 180 bit and 800 ms, respectively, were kept constant. The experimental results indicated that the splice loss of 1.01 dB at 20 μm offset to the left is lower than that of 2.6 dB at no offset and 4.1 dB at the right offset.
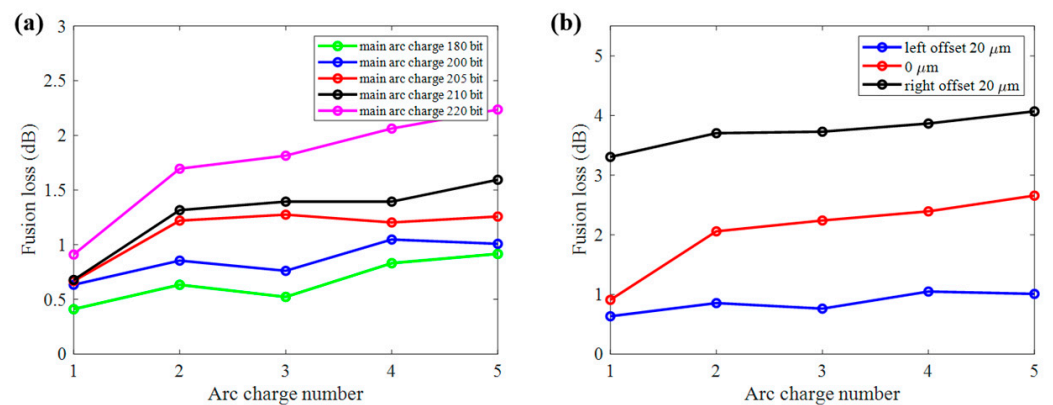

Figure 5. Splice loss measurement of the (**a**) main discharge intensities and times and (**b**) fiber offset and discharge times.

　　The total loss of this lensed fiber is approximately 1.8 dB at 915 nm, primarily due to the coupling losses between the CL and DC-ARF, the transmission loss in the 1 m DC-ARF, and fusion losses between the DC-ARF and LCF. The optimized fusion loss of 1.01 dB between the DC-ARF and LCF also causes approximately 21% transmission loss for the fluorescence signal reverse transmission. As shown in Figure 6a, the far-field output NA test of the lensed fiber (also the imaging NA) is performed by measuring the $1/e^2$ diameter of the output spot at different locations (Photon NanoScan, Ophir Optronics Solutions, Darmstadt, Germany). The experimental NA results in the *X* and *Y* directions are 0.11 and 0.095, respectively. The variability of the two axes of NA may be influenced by the inconsistency of the surface shape of the curved lens fabricated by the arc discharge. As shown in Figure 6b, the near-field output spot full-width at half maximum (FWHM) of the lensed fiber is also measured. The 20× objective (Plan N, Olympus, Tokyo, Japan) and a 250 mm plano-convex lens (GCL-010803, Daheng Optics, Beijing, China) form a 14.7× spot magnification system, and the measured near-field FWHM of the lensed fiber is 3.65 μm. The working distance of the lensed fiber is obtained by subtracting the hemisphere radius of the lensed fiber surface from the distance between surface S_1 and S_2 (illustrated in Figure 2), and the working distance is approximately 260 μm.
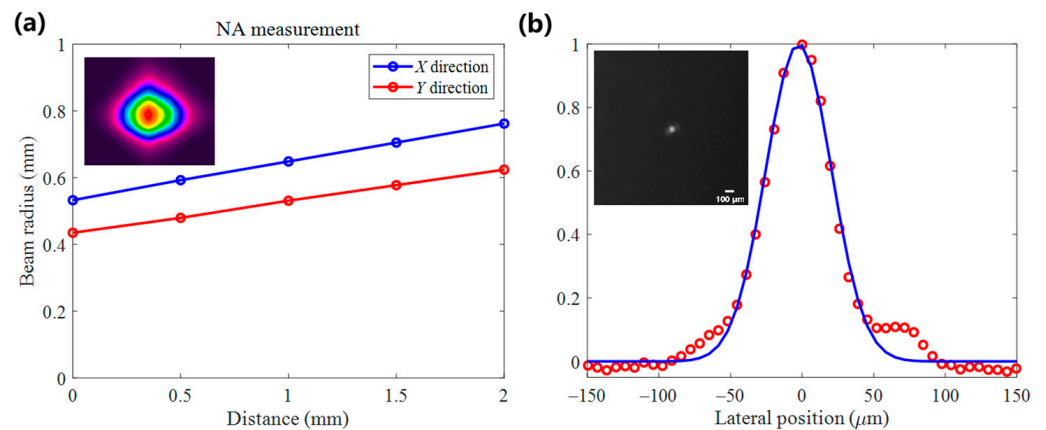
Figure 6. (**a**) Lensed fiber far-field NA measurement. The inset figure in the upper left is the Gaussian beam spot measured at the lensed fiber output. (**b**) Lensed-fiber near-field spot measurement. Red circle: measured data; Blue line: Gaussian fit. The inset figure in the upper left is the Gaussian beam measured by CMOS camera after the convergence of the lensed fiber. The scale bar is 100 μm.

3. Experimental Results

In the experimental results, we first evaluate the maximum FOV and lateral resolution of the objective-lens-free TPEM probe. A square standard grid with a side length of 50 μm is used for the FOV testing. The maximum FOV is 750 μm (*X* axis at ±93.75 V driving voltage and *Y* axis at ±71.25 V driving voltage), as shown in Figure 7a. An uneven intensity distribution image in parts is mainly due to the influence of off-axis aberrations such as field curvature and grid standard fabrication by uneven coating fluorescent microbeads. Green fluorescent polymer microspheres (G400 Fluoro-max, Thermo Scientific, Waltham, MA, USA) measuring 380 nm were chosen for the full width at half-maximum (FWHM) of point spread function (PSF) measurement. The lateral resolution, calculated from the Gaussian fit curve, is 3.03 μm, as shown in Figure 7b.
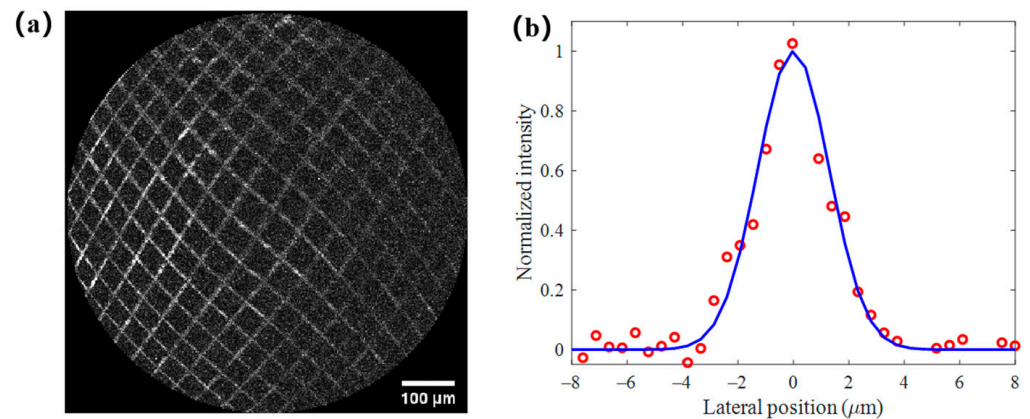

Figure 7. (**a**) Two-photon imaging of a 50 μm square standard grid for FOV measurement. Scale bar: 100 μm; and (**b**) Two-photon imaging lateral resolution measurement. Red circle: measured data; Blue line: Gaussian fit.

The two-photon endomicroscopic imaging of ex vivo organs, such as the heart, kidney, brain, and stomach wall, of an eGFP-labeled (enhanced green fluorescent protein) mouse was first performed to verify the enlarged FOV imaging capability. Figure 8a illustrates the heart muscle with long cardiomyocyte structures (the power under the probe is 65 mW, 10 frames averaged), and some regions of the cardiomyocyte structures have a similar orientation. Figure 8b illustrates the kidney tissue with distinguishable renal tubules (90 mW, 20 frames averaged). Figure 8c,d show the two-photon imaging of the brain tissue in two different FOVs (90 mW, 10 frames averaged), and white arrows indicate micro

brain blood vessels. The results of the inner gastric walls at depths of 20 μm, 70 μm, and 120 μm are shown in Figure 8e–g. The white arrow illustrates the structure of the gastric pit in the mucosal layer of the gastric wall (80 mW, 30 frames averaged). The in vivo brain imaging results of a 10-week-old Thy1-YFP-labeled (yellow fluorescent protein) mouse is also depicted in Figure 8h (100 mW, 30 frames averaged), from which neural cell bodies can be obtained. The mouse is craniotomized to remove the skull by handheld cranial drill (RWD Life Science, Shenzhen, China), its body is fixed to a customized body fixator for stable imaging, and this lensed fiber-optic nonlinear endoscopic probe is placed on the craniotomized brain region for in vivo two-photon fluorescence imaging. The ex vivo and in vivo two-photon imaging results above have demonstrated objective-lens-free lensed fiber-optic TPEM with an enlarged FOV capability at subcellular resolution. The current imaging NA of the lensed fiber leads to a reduction in image signal-to-noise background (SNR). Subsequent improvements around the imaging NA will result in higher SNR and collection efficiency. We will further discuss the options for NA enhancement in the discussion section.
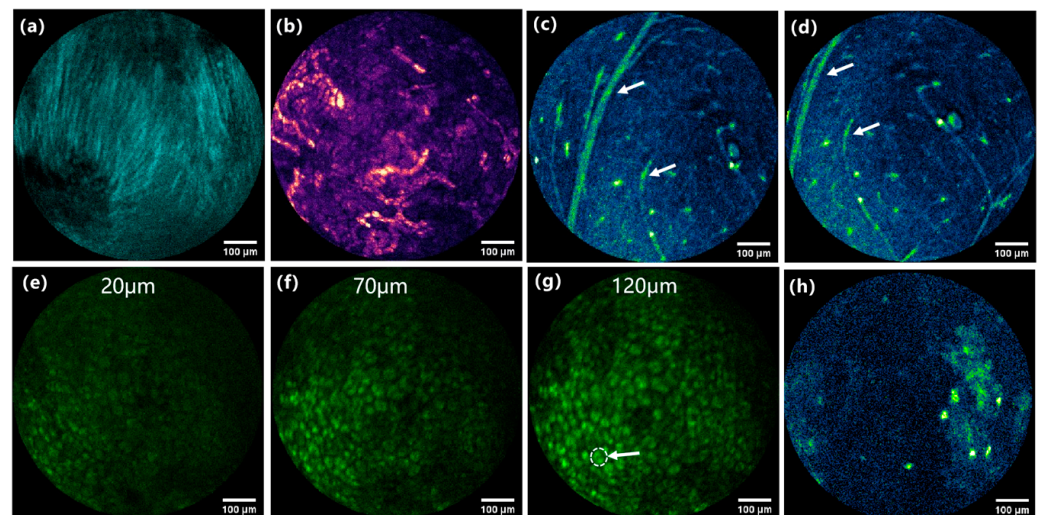

Figure 8. TPEM imaging results: (**a**) heart; (**b**) kidney; (**c**,**d**) brain tissue; (**e**–**g**) stomach inner wall tissue at 20 μm, 70 μm, and 120 μm depths; and (**h**) in vivo brain tissue. Scale bars: 100 μm.

4. Discussion

This work has proposed a lensed fiber-optic two-photon endomicroscopy probe for field-of-view enhancement. We point out that the technical advantage of this lensed fiber scanning scheme is the use of curved hemisphere surfaces for convergence, so that the actual scanning range of the PZT scanner (D_{scan}) is the final imaging FOV. Compared to imaging through an M-fold microscope objective, there is an M-fold enhancement in the FOV at the same PZT driving voltage; therefore, a FOV enhancement can be obtained. Considering that the spiral scanning is a circular FOV, the imaging throughput of this TPEM probe can be calculated by Equation (7) [20,25,41]:

$$Throughput \approx \frac{\pi}{4} \left(\frac{FOV}{\delta_{PSF}} \right)^2 = 48095.7 \qquad (10)$$

Compared with our previous work on TPEM based on DC-ARF with 3× objective [29] and microsphere-spliced DC-ARF with 3× objective [20], the imaging throughput of this objective-lens-free TPEM scheme is increased by 14.7 times and 2.3 times, respectively. Compared to the integrated rigid length of TPEM, which is 49.1 mm with 3× objective [20], the integrated probe has an integrated rigid length of 33.1 mm, which is 31.8% smaller than that of TPEM. Additionally, this objective-lens-free, lensed fiber-optic TPEM scheme can lower the assembly difficulty and integrated probe cost. In the future, the following

approaches can be considered for the resolution improvement of this objective-lens-free imaging scheme while maintaining the FOV enhancement capability. First, the development of double-cladding photonic bandgap fibers can improve the fiber NA and thus improve the output imaging NA. Second, by using advanced micro- and nano-fabrication techniques to fabricate ultracompact objectives (GRIN lens [25]/aspherical microlens [42]) to the fiber end face, a higher output NA can also be achieved [43]. The above two schemes can further improve the imaging resolution and expand the imaging throughput in the PZT scanning endoscopy system.

Additionally, our current miniature TPEM probe has a 5.8 mm integration diameter, which is mainly due to the current PZT outer diameter (3.2 mm). Using a PZT with a smaller outer diameter (1 mm), the assembled probe diameter can be less than 2.8 mm. The fabrication of a forward-fixed PZT fiber scanner with a shorter cantilever length [44] and active braking for the PZT scanner driving signals [45] can be integrated into this lensed fiber-optic scheme to improve the imaging speed and provide an objective-lens-free fiber scanning imaging scheme to achieve neuron dynamics imaging in freely behaving animals [46].

5. Conclusions

In summary, we proposed an objective-lens-free, lensed fiber-optic TPEM for field-of-view enhancement. The two-photon endomicroscopic probe had an FOV of 750 μm and a lateral resolution of 3.03 μm. To validate the FOV enhancement capability, we performed ex vivo and in vivo experiments on biological tissues. The lensed fiber-optic TPEM present promising opportunities for internal organ imaging and freely behaving brain imaging in the biomedical field.

Author Contributions: Conceptualization, C.W. and L.F.; methodology, C.W., H.L., J.M., Q.F., Y.L., Y.C., Y.G., J.T. and X.L.; Validation, C.W.; software, C.W. and J.M.; writing—original draft preparation, C.W. and H.L.; writing—review and editing, C.W., H.L., F.Y., C.Z., R.W., A.W. and L.F.; supervision, A.W. and L.F.; project administration, A.W. and L.F.; funding acquisition, A.W. and L.F. All authors have read and agreed to the published version of the manuscript.

Institutional Review Board Statement: All procedures were approved by Peking University Animal Use and Care Committee and complied with the standards of the Association for Assessment and Accreditation of Laboratory Animal Care (protocol code: SYXK2019-0032; date of approval: 1 November 2021).

Informed Consent Statement: Not applicable.

Data Availability Statement: Not applicable.

Conflicts of Interest: The authors declare no conflict of interest.

References

1. Denk, W.; Strickler, J.H.; Webb, W.W. Two-photon laser scanning fluorescence microscopy. *Science* **1990**, *248*, 73–76. [CrossRef]
2. Zipfel, W.R.; Williams, R.M.; Webb, W.W. Nonlinear magic: Multiphoton microscopy in the biosciences. *Nat. Biotechnol.* **2003**, *21*, 1369–1377. [CrossRef] [PubMed]
3. Helmchen, F.; Fee, M.S.; Tank, D.W.; Denk, W. A miniature head-mounted two-photon microscope: High-resolution brain imaging in freely moving animals. *Neuron* **2001**, *31*, 903–912. [CrossRef] [PubMed]
4. Klioutchnikov, A.; Wallace, D.J.; Frosz, M.H.; Zeltner, R.; Sawinski, J.; Pawlak, V.; Voit, K.M.; Russell, P.S.J.; Kerr, J.N.D. Three-photon head-mounted microscope for imaging deep cortical layers in freely moving rats. *Nat. Methods* **2020**, *17*, 509–513. [CrossRef]
5. Zong, W.; Wu, R.; Chen, S.; Wu, J.; Wang, H.; Zhao, Z.; Chen, G.; Tu, R.; Wu, D.; Hu, Y.; et al. Miniature two-photon microscopy for enlarged field-of-view, multi-plane and long-term brain imaging. *Nat. Methods* **2021**, *18*, 46–49. [CrossRef] [PubMed]
6. Li, A.; Guan, H.; Park, H.C.; Yue, Y.; Chen, D.; Liang, W.; Li, M.; Lu, H.; Li, X. Twist-free ultralight two-photon fiberscope enabling neuroimaging on freely rotating/walking mice. *Optica* **2021**, *8*, 870–879. [CrossRef]

7. Fu, L.; Jain, A.; Xie, H.; Cranfield, C.; Gu, M. Nonlinear optical endoscopy based on a double-clad photonic crystal fiber and a MEMS mirror. *Opt. Express* **2006**, *14*, 1027–1032. [CrossRef] [PubMed]
8. Tang, S.; Jung, W.; McCormick, D.; Xie, T.; Su, J.; Ahn, Y.C.; Tromberg, B.J.; Chen, Z. Design and implementation of fiber-based multiphoton endoscopy with microelectromechanical systems scanning. *J. Biomed. Opt.* **2009**, *14*, 034005. [CrossRef]
9. Duan, X.; Li, H.; Qiu, Z.; Joshi, B.P.; Pant, A.; Smith, A.; Kurabayashi, K.; Oldham, K.R.; Wang, T.D. MEMS-based multiphoton endomicroscope for repetitive imaging of mouse colon. *Biomed. Opt. Express* **2015**, *6*, 3074–3083. [CrossRef]
10. Myaing, M.T.; MacDonald, D.J.; Li, X. Fiber-optic scanning two-photon fluorescence endoscope. *Opt. Lett.* **2006**, *31*, 1076–1078. [CrossRef]
11. Rivera, D.R.; Brown, C.M.; Ouzounov, D.G.; Pavlova, I.; Kobat, D.; Webb, W.W.; Xu, C. Compact and flexible raster scanning multiphoton endoscope capable of imaging unstained tissue. *Proc. Natl Acad. Sci. USA* **2011**, *108*, 17598–17603. [CrossRef] [PubMed]
12. Do, D.; Yoo, H.; Gweon, D.G. Fiber-optic raster scanning two-photon endomicroscope using a tubular piezoelectric actuator. *J. Biomed. Opt.* **2014**, *19*, 066010. [CrossRef] [PubMed]
13. Ducourthial, G.; Leclerc, P.; Mansuryan, T.; Fabert, M.; Brevier, J.; Habert, R.; Braud, F.; Batrin, R.; Bizet, C.V.; Heckly, G.B.; et al. Development of a real-time flexible multiphoton microendoscope for label-free imaging in a live animal. *Sci. Rep.* **2015**, *5*, 18303. [CrossRef] [PubMed]
14. Liang, W.; Hall, G.; Messerschmidt, B.; Li, M.J.; Li, X. Nonlinear optical endomicroscopy for label-free functional histology in vivo. *Light Sci. Appl.* **2017**, *6*, e17082. [CrossRef]
15. Lombardini, A.; Mytskaniuk, V.; Sivankutty, S.; Andresen, E.R.; Chen, X.; Wenger, J.; Fabert, M.; Joly, N.; Louradour, F.; Kudlinski, A.; et al. High-resolution multimodal flexible coherent Raman endoscope. *Light Sci. Appl.* **2018**, *7*, 10. [CrossRef]
16. Kim, D.Y.; Hwang, K.; Ahn, J.; Seo, Y.H.; Kim, J.B.; Lee, S.; Yoon, J.H.; Kong, E.; Jeong, Y.; Jon, S.; et al. Lissajous scanning two-photon endomicroscope for in vivo tissue imaging. *Sci. Rep.* **2019**, *9*, 3560. [CrossRef]
17. Kudlinski, A.; Cassez, A.; Vanvincq, O.; Septier, D.; Pastre, A.; Habert, R.; Baudelle, K.; Douay, M.; Mytskaniuk, V.; Tsvirkun, V.; et al. Double clad tubular anti-resonant hollow core fiber for nonlinear microendoscopy. *Opt. Express* **2020**, *28*, 15062–15070. [CrossRef]
18. Guan, H.; Liang, W.; Li, A.; Gau, Y.A.; Chen, D.; Li, M.J.; Bergles, D.E.; Li, X. Multicolor fiber-optic two-photon endomicroscopy for brain imaging. *Opt. Lett.* **2021**, *46*, 1093–1096. [CrossRef]
19. Septier, D.; Mytskaniuk, V.; Habert, R.; Labat, D.; Baudelle, K.; Cassez, A.; Brévalle-Wasilewski, G.; Conforti, M.; Bouwmans, G.; Rigneault, H.; et al. Label-free highly multimodal nonlinear endoscope. *Opt. Express* **2022**, *30*, 25020–25033. [CrossRef]
20. Wang, C.; Liu, H.; Cui, H.; Ma, J.; Li, Y.; Tian, J.; Jin, C.; Chen, Y.; Gao, Y.; Fu, Q.; et al. Two-photon endomicroscopy with microsphere-spliced double-cladding antiresonant fiber for resolution enhancement. *Opt. Express* **2022**, *30*, 26090–26101. [CrossRef]
21. Tang, Y.; Anandasabapathy, S.; Richards-Kortum, R. Advances in optical gastrointestinal endoscopy: A technical review. *Mol. Oncol.* **2021**, *15*, 2580–2599. [CrossRef] [PubMed]
22. Chen, D.; Nauen, D.W.; Park, H.C.; Li, D.; Yuan, W.; Li, A.; Guan, H.; Kut, C.; Chaichana, K.L.; Bettegowda, C.; et al. Label-free imaging of human brain tissue at subcellular resolution for potential rapid intra-operative assessment of glioma surgery. *Theranostics* **2021**, *11*, 7222. [CrossRef] [PubMed]
23. Ryu, S.Y.; Choi, H.Y.; Na, J.; Choi, W.J.; Lee, B.H. Lensed fiber probes designed as an alternative to bulk probes in optical coherence tomography. *Appl. Opt.* **2008**, *47*, 1510–1516. [CrossRef]
24. Qiu, Y.; Wang, Y.; Belfield, K.D.; Liu, X. Ultrathin lensed fiber-optic probe for optical coherence tomography. *Biomed. Opt. Express* **2016**, *7*, 2154–2162. [CrossRef] [PubMed]
25. Liang, W.; Park, H.C.; Li, K.; Li, A.; Chen, D.; Guan, H.; Yue, Y.; Gau, Y.A.; Bergles, D.E.; Li, M.J.; et al. Throughput-speed product augmentation for scanning fiber-optic two-photon endomicroscopy. *IEEE Trans. Med. Imaging* **2020**, *39*, 3779–3787. [CrossRef]
26. Bao, H.; Gu, M. A 0.4-mm-diameter probe for nonlinear optical imaging. *Opt. Express* **2009**, *17*, 10098–10104. [CrossRef] [PubMed]
27. Akhoundi, F.; Qin, Y.; Peyghambarian, N.; Barton, J.K.; Kieu, K. Compact fiber-based multi-photon endoscope working at 1700 nm. *Biomed. Opt. Express* **2018**, *9*, 2326–2335. [CrossRef]
28. Kim, J.B.; Jeon, J.; Hwang, K.; Kim, D.Y.; Jeong, K. Objective-lens-free confocal endomicroscope using Lissajous scanning lensed-fiber. *J. Opt. Microsyst.* **2021**, *1*, 034501. [CrossRef]
29. Wang, C.; Liu, H.; Ma, J.; Cui, H.; Li, Y.; Wu, D.; Hu, Y.; Wu, D.; Fu, Q.; Liang, L.; et al. Spiral scanning fiber-optic two-photon endomicroscopy with a double-cladding antiresonant fiber. *Opt. Express* **2021**, *29*, 43124–43135. [CrossRef]
30. Cui, H.; Wang, C.; Ma, J.; Liu, H.; Wu, D.; Wang, A.; Feng, L. Forward-detection fiber scanning endomicroscopy for two-photon fluorescence. In *OSA Biophotonics Congress: Optics in the Life Sciences*; Optica Publishing Group: Washington, DC, USA, 2021; p. JTu4a.21.
31. Wang, C.; Liu, H.; Ma, J.; Cui, H.; Tian, J.; Fu, Q.; Wu, R.; Wang, A.; Feng, L. Flexible two-photon endomicroscope probe with double-cladding antiresonant fiber. In *Imaging Systems and Applications*; Optica Publishing Group: Vancouver, BC, Canada, 2022; p. JW2A.
32. Wang, C.; Zhang, X.; Liu, H.; Ma, J.; Tian, J.; Fu, Q.; Wu, R.; Wang, A.; Feng, L. Modeling and analysis of reverse-fixed piezoelectric tube fiber scanner for two-photon endomicroscopy. In *AOPC 2022: Biomedical Optics*; SPIE: Beijing, China, 2023; Volume 12560, pp. 47–52.
33. Zhang, N.; Tsai, T.H.; Ahsen, O.O.; Liang, K.; Lee, H.C.; Xue, P.; Li, X.; Fujimoto, J.G. Compact piezoelectric transducer fiber scanning probe for optical coherence tomography. *Opt. Lett.* **2014**, *39*, 186–188. [CrossRef]

34. Wei, C.; Weiblen, R.J.; Menyuk, C.R.; Hu, J. Negative curvature fibers. *Adv. Opt. Photonics* **2017**, *9*, 504–561. [CrossRef]
35. Ni, W.; Yang, C.; Luo, Y.; Xia, R.; Lu, P.; Hu, D.J.J.; Danto, S.; Shum, P.P.; Wei, L. Recent advancement of anti-resonant hollow-core fibers for sensing applications. *Photonics* **2021**, *8*, 128. [CrossRef]
36. Kong, G.J.; Kim, J.; Choi, H.Y.; Im, J.E.; Park, B.H.; Paek, U.C.; Lee, B.H. Lensed photonic crystal fiber obtained by use of an arc discharge. *Opt. Lett.* **2006**, *31*, 894–896. [CrossRef]
37. Chen, Y.; Wang, C.; Xiao, L. Ultrathin lensed photonic crystal fibers with wide bandwidth and long working distances. *J. Lightw. Technol.* **2021**, *39*, 2482–2488. [CrossRef]
38. Xiao, L.; Jin, W.; Demokan, M.S. Fusion splicing small-core photonic crystal fibers and single-mode fibers by repeated arc discharges. *Opt. Lett.* **2007**, *32*, 115–117. [CrossRef]
39. Chong, J.H.; Rao, M.K. Development of a system for laser splicing photonic crystal fiber. *Opt. Express* **2003**, *11*, 1365–1370. [CrossRef]
40. Min, Y.; Filipkowski, A.; Stępniewski, G.; Dobrakowski, D.; Zhou, J.; Lou, B.; Klimczak, M.; Zhao, L.; Buczyński, R. Fusion splicing of silica hollow core anti-resonant fibers with polarization maintaining fibers. *J. Lightw. Technol.* **2021**, *39*, 3251–3259. [CrossRef]
41. Rivera, D.R.; Brown, C.M.; Ouzounov, D.G.; Webb, W.W.; Xu, C. Use of a lensed fiber for a large-field-of-view, high-resolution, fiber-scanning microendoscope. *Opt. Lett.* **2012**, *37*, 881–883. [CrossRef]
42. Wang, B.; Zhang, Q.; Gu, M. Aspherical microlenses enabled by two-photon direct laser writing for fiber-optical microendoscopy. *Opt. Mater. Express* **2020**, *10*, 3174–3184. [CrossRef]
43. Gissibl, T.; Thiele, S.; Herkommer, A.; Giessen, H. Two-photon direct laser writing of ultracompact multi-lens objectives. *Nat. Photonics* **2016**, *10*, 554–560. [CrossRef]
44. Park, H.; Guan, H.; Li, A.; Yue, Y.; Li, M.; Li, X. High-speed fiber-optic scanning nonlinear endomicroscopy for imaging neuron dynamics in vivo. *Opt. Lett.* **2020**, *45*, 3605–3608. [CrossRef] [PubMed]
45. Lee, C.M.; Engelbrecht, C.J.; Soper, T.D.; Helmchen, F.; Seibel, E.J. Scanning fiber endoscopy with highly flexible, 1 mm catheterscopes for wide-field, full-color imaging. *J. Biophoton.* **2010**, *3*, 385–407. [CrossRef] [PubMed]
46. Yu, X.; Zhou, L.; Qi, T.; Zhao, H.; Xie, H. MEMS Enabled Miniature Two-Photon Microscopy for Biomedical Imaging. *Micromachines* **2023**, *14*, 470. [CrossRef] [PubMed]